PAPER

Check for updates

Experimental and theoretical study of novel aminobenzamide–aminonaphthalimide fluorescent dyads with a FRET mechanism†

Ángel L. García,[a] Adrián Ochoa-Terán, [ID] *[a] Antonio Tirado-Guízar,[a] Jesús Jara-Cortés, [ID] *[b] Georgina Pina-Luis,[a] Hisila Santacruz Ortega,[c] Victoria Labastida-Galván,[d] Mario Ordoñez[d] and Jorge Peón [ID] [e]

In this work, both experimental and theoretical methods were used to study the photophysical and metal ion binding properties of a series of new aminobenzamide–aminonaphthalimide (2ABZ–ANAPIM) fluorescent dyads. The 2-aminobenzamide (2ABZ) and 6-aminonaphthalimide (ANAPIM) fluorophores were linked through alkyl chains (C_2 to C_6) to obtain four fluorescent dyads. These dyads present a highly efficient (0.61 to 0.98) Förster Resonant Energy Transfer (FRET) from the 2ABZ to the ANAPIM due to the 2ABZ emission and ANAPIM excitation band overlap and the configurational stacking of both aromatic systems which allows the energy transfer. These dyads interact with Cu^{2+} and Hg^{2+} metal ions in solution inhibiting the FRET mechanism by the cooperative coordination of both 2ABZ and ANAPIM moieties. Both experimental and theoretical results are consistent and describe clearly the photophysical and coordination properties of these new dyads.

Introduction

Nowadays one of the main problems worldwide is population growth. It is known that the world population amounted to 2529 million in 1950 and it will be 9700 million in 2050.[1] The population growth is intrinsically related to the consumption of natural resources, especially water. The data from the World Water Assessment Programme (WWAP) indicate that 2 million tons of garbage are dumped into the sea every day, and 70% of industrial waste is dumped without a prior treatment. Some of these pollutants are heavy metals, in particular Hg^{2+}, Pb^{2+}, Cu^{2+} and Co^{2+}. The major risk of heavy metals is that they are not chemically or biologically degradable and cause health problems such as intoxication, blindness, amnesia and sometimes death, in relatively high concentrations.[2]

Especially, Hg^{2+} ion is one of the most toxic and prevalent heavy metals, it is widely distributed by air, water and soil with cumulative and persistent characteristics, it causes damage in DNA, alterations in cell mitosis and defects in the nervous system.[3] On the other hand, has been reported that a short time exposure to high concentrations of Cu^{2+} may result in anemic brain disorders, while a long-term exposure causes hepatic cirrhosis or perception of a nerve barrier.[4] Therefore, more efficient, economical and viable techniques for detection and removal of heavy metals are desirable. A promising alternative for selective detection and extraction of heavy metals are the fluorescent chelating compounds, known as chemosensors, because they have several advantages such as simplicity, low-cost instrumentation, and the ability to be used for real-time monitoring.[5,6]

A common challenge in developing new fluorescent chemosensors is to find chemically stable fluorophores under the analysis conditions. The 1,8-naphthalimide (NAPIM) and 6-amino-1,8-naphthalimide (ANAPIM) fluorophores have been widely studied and applied in the design of fluorescent chemosensors due to its excellent photophysical properties such as high quantum yield, excitation and emission wavelengths at the visible spectrum, and high photo- and chemo-stability, among others.[7–9]

In literature there are reports regarding the design and study of naphthalimide based chemosensors for the detection of metal ions and anions as well as pH measurements. Anbu and

[a]*Centro de Graduados e Investigación en Química, Tecnológico Nacional de México/IT de Tijuana, Tijuana, Baja California, Mexico. E-mail: adrian.ochoa@tectijuana.edu.mx*

[b]*Unidad Académica de Ciencias Básicas e Ingenierías, Universidad Autónoma de Nayarit, Tepic, Nayarit, Mexico. E-mail: josejc@uan.edu.mx*

[c]*Departamento de Investigación en Polímeros y Materiales, Universidad de Sonora, Hermosillo, Sonora, Mexico*

[d]*Centro de Investigaciones Químicas-(IICBA), Universidad Autónoma del Estado de Morelos, Cuernavaca, Morelos, Mexico*

[e]*Instituto de Química, Universidad Nacional Autónoma de México, Ciudad de México, Mexico*

† Electronic supplementary information (ESI) available: MS data; ^{1}H NMR, ^{13}C NMR, FTIR and electronic absorption and emission spectra of relevant compounds, as well as additional information from the calculations. See DOI: 10.1039/d1ra09278b

coworkers developed a new naphthalimide–phenanthroimidazole fluorescent chemosensor for a turn-ON Cu^{2+} detection in living cancer cells,[10] and a naphthalimide-aza 18-crown-6 ether ion-selective chemosensor for UO_2^{2+} ion was reported by Tsukahara.[11] A ratiometric 4-amido-1,8-naphthalimide fluorescent sensor based on excimer-monomer emission for determination of pH and water content in organic solvents was reported by Bojinov and coworkers.[12] Zhang and coworkers developed a novel naphthalimide–glutathione chemosensor for fluorescent detection of Fe^{3+} and Hg^{2+} in aqueous medium[13] and the green synthesis of fluorescent N,O-chelating hydrazone Schiff base for multi-analyte sensing in Cu^{2+}, F^- and CN^- ions was reported by Ervithayasuporn.[14] Also, a highly Al^{3+}-selective fluorescence probe based on naphthalimide-Schiff base and its application to practical water samples was reported by Whu and coworkers.[15] Zhang and coworkers[16] developed a selective chemosensor for Cu^{2+} ion, where ANAPIM is connected to a dihydroxibenzylimine receptor. This chemosensor displays an ON/OFF fluorescent response in a buffered aqueous media at pH 7.2. A 1 : 2 metal–ligand ratio was established for the supramolecular complex. Finally, they concluded that the quenching of fluorescence is due to the intrinsic strong paramagnetic effect of Cu^{2+} ion. Pachenko and coworkers[17] designed a selective chemosensor for Ca^{2+} ion detection connecting the ANAPIM fluorophore to an aza-15-crown-5 ether in two different fashions to modulate the fluorescent response.

A fluorescent dyad with an ICT-PET-FRET mechanism acting as a pH sensor was studied by Baoli and coworkers (Fig. 1a),[18] using coumarin and ANAPIM chromophores as energy donor and acceptor to improve the FRET mechanism, connecting a morpholine group to ANAPIM inducing a PET process. Theoretical calculations showed that the HOMO of morpholine is in −5.4 eV and the HOMO of ANAPIM is −5.71 eV, which favors the PET from morpholine to ANAPIM. Coumarin and morpholine groups are sensible to pH and into acid environment the morpholine is protonated inhibiting the PET process

allowing the FRET from coumarin to ANAPIM with an emission at 525 nm. On the contrary, in a basic medium the coumarin is deprotonated inducing an ICT and emitting at 467 nm. This work demonstrated the ability of ANAPIM chromophore as energy acceptor in a FRET process.

Previously, we studied the photophysical properties and sensing behavior towards metal ions of a series of aminobenzamide–naphthalimide fluorescent dyads (2ABZ–NAPIM) with ICT-PET fluorescent mechanisms (Fig. 1b).[19] In these dyads the exciting and emission wavelengths of both fluorophores are similar emitting around 400 nm. Interestingly, the fluorescence intensity of 2ABZ–NAPIM dyads was dependent on the spacer length and their quantum yield were lower than the individual fluorophores, which was attributed to a PET process. This PET was analyzed by theoretical methods finding that the HOMO of NAPIM and 2ABZ are at −6.98 eV and −5.47 eV respectively, indicating an electronic transfer from 2ABZ to NAPIM. Electrochemical analysis also confirmed the direction of this process. These dyads were sensitive towards two metal ions such as Hg^{2+} and Cu^{2+} inhibiting the PET in the shorter dyads and showing an OFF/ON fluorescent response by the increasing emission of NAPIM fluorophore and inhibition of an ICT in the 2ABZ. The NMR analysis demonstrated the interaction of the metal ions in the 2ABZ is through the amine and amide functional groups, as it was previously reported by other authors.[20-22] Some fluorescent dyads containing a naphthalimide (NAPIM) and dansylamide (DANS) fluorophores linked by a polymethylene spacer were reported by Pischel (Fig. 1c).[23] This work describes a singlet–singlet energy transfer (SSET) and PET processes between NAPIM and DANS. Both processes were affected by the presence of protons quenching DANS and enhancing NAPIM fluorescence. Ramaiah and collaborators[24] found that the presence of Cu^{2+} and Zn^{2+} has the same quenching effect in the dyads with shorter spacing length due to the SSET and PET processes, instead a FRET process occurs in dyads with longer oligomethylene chain (six and eight methylenes).[25]

In this work new 2ABZ–ANAPIM dyads with an ICT-FRET mechanism were synthesized and evaluated against metal ions varying the distance between both fluorophores to optimize the resonant energy transfer as well as, to study the detection of metal ions (Fig. 1d). Additionally, the experimental results are complemented by excited state calculations in order to rationalize the photophysical mechanism of the dyads, as well as the changes in their optical response after complexation with metal ions.

Experimental section

Materials

All chemical reagents were purchased from a commercial supplier and were employed as received without further purification.

Measurements

^{1}H NMR spectra were recorded in a 400 MHz Brucker Advance III NMR spectrophotometer; the samples were dissolved in
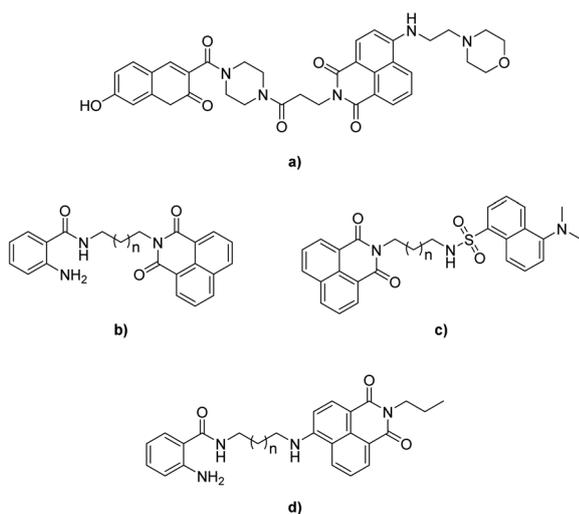

Fig. 1 Chemical structure of (a) coumarin–ANAPIM, (b) 2ABZ–NAPIM, (c) NAPIM–DANS and (d) 2ABZ–ANAPIM fluorescent dyads.

DMSO-d$_6$ containing small amounts of TMS as the internal standard. FTIR spectra were recorded using a PerkinElmer spectrophotometer Spectrum 400 in the range from 4000 to 600 cm^{-1}. MS (FAB+) HRMS analysis were recorded in an MStation JMS-700 JEOL. Optical properties of NDIs were analyzed by UV-Vis and fluorescence spectroscopy, recorded in a UV-Vis Spectrophotometer of double beam Shimadzu model UV2700 and a Varian Fluorescence Spectrophotometer model Eclipse Cary.

Synthesis

6-Bromo-2-propyl-1*H*-benzo[*de*]isoquinoline-1,3(2*H*)-dione (1). In a 50 mL round bottom flask with magnetic stirring the 4-bromo-1,8-naphtoic anhydride (500 mg, 1.8 mmol) was dissolved in ethanol (25 mL), propylamine (1.8 mmol) was added and the mixture was refluxed during 16 h. Then the reaction mixture was cooled to room temperature until a solid was observed. The solid was filtered and washed with cold ethanol and dried at RT. Brown solid, 459 mg, 1.44 mmol, 80% yield.

^{1}H NMR (DMSO-d$_6$, 400 MHz): δ 8.68 (dd, J = 7.3, 1.2 Hz, 1H), 8.59 (dd, J = 8.5, 1.2 Hz, 1H), 8.44 (d, J = 7.9 Hz, 1H), 8.06 (d, J = 7.9 Hz, 1H), 7.87 (dd, J = 8.5, 7.3 Hz, 1H), 4.21–4.12 (m, 2H), 1.87–1.72 (m, 2H), 1.04 (t, J = 7.5 Hz, 3H). ^{13}C NMR (DMSO-d$_6$, 101 MHz): δ 162.8, 132.5, 131.4, 131.2, 130.9, 129.7, 129.0, 128.7, 128.2, 122.7, 121.9, 41.3, 20.7, 11.3. MS (FAB+) *m/z*: 318 [M + H$^+$]. HRMS (FAB+): calculated for C$_{15}$H$_{13}$BrNO$_2$: 318.0130; found: 318.0147.

General method for the synthesis of compounds 2a–d. In a 50 mL round bottom flask with magnetic stirring the compound **1** (300 mg, 0.63 mmol) was dissolved in DMF (10 mL) and then was added the corresponding alkydiamine (30 molar equiv.). The mixture was stirred and heated at 110 °C for 3 h. Then, the mixture was cooled to RT and it was poured into 100 mL of cold water to form a solid. The solid was filtered and dried at RT, then it was recrystallized in toluene and dried at RT.

6-((2-Aminoethyl)amino)-2-propyl-1*H*-benzo[*de*]isoquinoline-1,3(2*H*)-dione (2a). Yellow solid, 194.3 mg, 71% yield. ^{1}H NMR (DMSO-d$_6$, 400 MHz): δ 8.62 (d, J = 8.5 Hz, 1H), 8.44 (d, J = 7.2 Hz, 1H), 8.27 (d, J = 8.5 Hz, 1H), 8.23 (s, 1H), 7.79 (t, J = 4.6 Hz, 1H), 7.70 (t, J = 7.7 Hz, 1H), 6.85 (d, J = 8.6 Hz, 1H), 3.99 (t, J = 7.6 Hz, 2H), 3.46 (ddd, J = 13.6, 7.8, 6.7 Hz, 4H), 1.63 (hxt, J = 7.4 Hz, 2H), 0.91 (t, J = 7.4 Hz, 3H). ^{13}C NMR (DMSO-d$_6$, 101 MHz): δ 163.4, 162.4, 150.9, 134.6, 131.1, 129.8, 128.8, 124.8, 122.4, 120.6, 108.5, 104.2, 43.0, 41.2, 36.5, 21.4, 11.9. MS (FAB+) *m/z*: 298 [M + H$^+$]. HRMS (FAB+): calculated for C$_{17}$H$_{20}$N$_3$O$_2$: 298.1556; found: 298.1562.

6-((3-Aminopropyl)amino)-2-propyl-1*H*-benzo[*de*]isoquinoline-1,3(2*H*)-dione (2b). Yellow solid, 246.2 mg, 86% yield. ^{1}H NMR (DMSO-d$_6$, 400 MHz): δ 8.69 (dd, J = 8.52, 0.84 Hz, 1H), 8.44 (dd, J = 7.28, 0.84 Hz, 1H), 8.28 (d, J = 8.52 Hz, 1H), 7.73 (t, J = 5.28 Hz, 1H), 7.69 (td, J = 8.32, 7.4 Hz, 1H), 6.80 (d, J = 8.6 Hz, 1H), 3.98 (t, J = 7.36 Hz, 2H), 3.41 (q, J = 6.64 Hz, 2H), 3.25 (q, J = 6.76 Hz, 2H), 1.87 (qnt, J = 6.96 Hz, 2H), 1.63 (m, 2H), 0.91 (t, J = 7.44 Hz, 3H). ^{13}C NMR (DMSO-d$_6$, 101 MHz): δ 163.4, 161.7, 151.0, 134.6, 131.1, 129.9, 128.9, 124.8, 122.4, 120.6, 108.2, 104.3, 41.2, 41.0, 35.6, 28.3, 21.4, 11.8. MS (FAB+) *m/z*: 312 [M +

H$^+$]. HRMS (FAB+): calculado para C$_{18}$H$_{22}$N$_3$O$_2$: 312.1712; found: 312.1724.

6-((4-Aminobutyl)amino)-2-propyl-1*H*-benzo[*de*]isoquinoline-1,3(2*H*)-dione (2c). Yellow solid, 122.2 mg, 41% yield. ^{1}H NMR (DMSO-d$_6$, 400 MHz): δ 8.70 (dd, J = 8.6, 1.2 Hz, 1H), 8.44 (dd, J = 7.4, 1.0 Hz, 1H), 8.27 (d, J = 8.5 Hz, 1H), 7.75 (t, J = 5.4 Hz, 1H), 7.68 (dd, J = 8.5, 7.3 Hz, 1H), 6.79 (d, J = 8.6 Hz, 1H), 4.98 (m, 2H), 3.40 (q, J = 6.6 Hz, 2H), 3.16 (m, 2H), 1.78–1.51 (m, 6H), 0.91 (t, J = 7.5 Hz, 3H). ^{13}C NMR (DMSO-d$_6$, 101 MHz): 163.4, 161.5, 151.1, 134.7, 131.1, 129.9, 129.0, 124.7, 122.4, 120.6, 108.0, 104.3, 42.9, 41.2, 37.3, 27.2, 25.7, 21.4, 11.8. MS (FAB+) *m/z*: 326 [M + H$^+$]. HRMS (FAB+): calculated for C$_{19}$H$_{24}$N$_3$O$_2$: 326.1869; found: 326.1874.

6-((6-Aminohexyl)amino)-2-propyl-1*H*-benzo[*de*]isoquinoline-1,3(2*H*)-dione (2d). Yellow solid, 144.7 mg, 74% yield. ^{1}H NMR (DMSO-d$_6$, 400 MHz): δ 8.71 (d, J = 8.4 Hz, 1H), 8.44 (d, J = 7.3 Hz, 1H), 8.27 (d, J = 8.5 Hz, 1H), 7.73 (d, J = 6.0 Hz, 1H), 7.68 (t, J = 7.9 Hz, 1H), 6.78 (d, J = 8.6 Hz, 1H), 3.98 (dd, J = 8.5, 6.3 Hz, 2H), 3.45 (q, J = 7.0 Hz, 2H), 3.38 (q, J = 6.6 Hz, 2H), 1.70 (q, J = 7.1 Hz, 2H), 1.62 (qnt, J = 7.4 Hz, 2H), 1.40 (m, 6H), 0.91 (t, J = 7.4 Hz, 3H). ^{13}C NMR (DMSO-d$_6$, 101 MHz): 163.4, 161.5, 151.1, 134.7, 131.09, 129.9, 129.0, 124.7, 122.3, 120.6, 108.0, 104.3, 42.9, 41.2, 37.3, 27.2, 25.7, 25.4, 21.4, 11.8. MS (FAB+) *m/z*: 354 [M + H$^+$]. HRMS (FAB+): calculated for C$_{21}$H$_{28}$N$_3$O$_2$: 354.2182; found: 354.2202.

General method for the synthesis of compounds 3a–d. In a 50 mL round bottom flask with magnetic stirring under inert atmosphere isatoic anhydride (1 molar equiv.) was dissolved in THF (20 mL) and TEA (300 μL) were added to the solution. Once the reactives were dissolved, compound **2** (100 mg, 1 molar equiv.) was added to the solution and the mixture was refluxed for 2 h. Finally, the solvent was removed under reduced pressure, the obtained solid was washed with petroleum ether (3 × 10 mL) and ethyl ether (3 × 10 mL).

2-Amino-*N*-(2-((1,3-dioxo-2-propyl-2,3-dihydro-1*H*-benzo[*de*]isoquinolin-6-yl)amino)ethyl)benzamide (3a). Yellow solid, 111.5 mg, 77% yield. FTIR: 3459, 3349, 3062, 2956, 1677, 1615, 1631, 1578, 1537 cm^{-1}. ^{1}H NMR (DMSO-d$_6$, 400 MHz): δ 8.65 (d, J = 8.6 Hz, 1H), 8.49 (t, J = 5.6 Hz, 1H), 8.45 (d, J = 7.2 Hz, 1H), 8.28 (d, J = 8.5 Hz, 1H), 7.94 (t, J = 8.5 Hz, 1H), 7.71 (t, J = 7.7 Hz, 1H), 7.48 (d, J = 7.9 Hz, 1H), 7.14 (t, J = 7.9 Hz, 1H), 6.93 (d, J = 8.6 Hz, 1H), 6.70 (d, J = 8.2 Hz, 1H), 6.51 (t, J = 7.5 Hz, 1H), 6.45 (s, 2H), 3.98 (t, J = 7.3 Hz, 2H), 3.55 (s, 4H), 1.63 (m, 2H), 0.91 (t, J = 7.4 Hz, 3H). ^{13}C NMR (DMSO-d$_6$, 101 MHz): δ 170.0, 164.2, 163.4, 151.0, 150.2, 134.6, 132.3, 131.1, 129.83, 128.8, 128.6, 124.8, 122.3, 120.6, 116.9, 115.1, 114.9, 108.3, 104.2, 43.1, 41.2, 38.1, 21.4, 11.8. MS (FAB+) *m/z*: 417 [M + H$^+$]. HRMS (FAB+): calculated for C$_{24}$H$_{25}$N$_4$O$_3$: 417.1927; found: 417.1947.

2-amino-*N*-(3-((1,3-dioxo-2-propyl-2,3-dihydro-1*H* benzo[*de*]isoquinolin-6-yl)amino)propyl)benzamide (3b). Yellow solid, 120.8 mg, 80% yield. FTIR: 3444, 3339, 3059, 2965, 1670, 1610, 1630, 1579, 1520 cm^{-1}. ^{1}H NMR (DMSO-d$_6$, 400 MHz): δ 8.70 (dd, J = 8.6, 1.1 Hz, 1H), 8.44 (dd, J = 7.3, 1.04 Hz, 1H), 8.32 (t, J = 5.5 Hz, 1H) 8.26 (d, J = 8.6 Hz, 1H), 7.82 (t, J = 5.5 Hz, 1H), 7.69 (dd, J = 8.4, 8.5 Hz, 1H), 7.48 (d, J = 8.0, 1.6 Hz, 1H), 7.13 (ddd, J = 8.4, 7.1, 1.6 Hz, 1H), 6.81 (d, J = 8.7 Hz, 1H), 6.68 (dd, J = 8.2, 1.2 Hz, 1H), 6.51 (dd, J = 8.0, 1.2 Hz, 1H), 6.38 (s, 2H), 3.97

(t, J = 7.4 Hz, 2H), 3.36 (q, J = 8.8, 15 Hz, 2H), 1.95 (qnt, J = 6.7, 13.6 Hz, 2H), 1.62 (m, 2H), 0.90 (t, J = 7.5 Hz, 3H). ^{13}C NMR (DMSO-d$_6$, 101 MHz): δ 170.1, 164.3, 163.4, 151.1, 150.2, 134.6, 132.4, 131.2, 129.9, 128.9, 128.6, 124.9, 122.4, 120.6, 116.8, 115.0, 114.8, 108.2, 104.1, 43.0, 41.2, 38.1, 28.3, 21.4, 11.8. MS (FAB+) m/z: 431 [M + H$^+$]. HRMS (FAB+): calculated for C$_{25}$H$_{27}$N$_4$O$_3$: 431.2083. Found: 431.2103.

2-Amino-N-(4-((1,3-dioxo-2-propyl-2,3-dihydro-1H benzo[de] isoquinolin-6-yl)amino)butyl)benzamida (3c). Yellow solid, 140.9 mg, 80% yield. FTIR: 3444, 3339, 3059, 2965, 1670, 1610, 1630, 1579, 1520 cm^{-1}. ^{1}H NMR (DMSO-d$_6$, 400 MHz): δ 8.66 (d, J = 8.5 Hz, 1H), 8.38 (d, J = 7.2 Hz, 1H), 8.21 (s, 1H) 8.18 (d, J = 8.3 Hz, 1H), 7.87 (d, J = 7.9 Hz, 1H), 7.75 (t, J = 6.5, 1H), 7.40 (d, J = 7.7 Hz, 1H), 7.20 (t, J = 7.6 Hz, 1H), 6.76 (d, J = 8.6 Hz, 1H), 6.63 (d, J = 8.3 Hz, 1H), 6.44 (t, J = 7.4 Hz, 1H), 6.33 (s, 2H), 3.93 (t, J = 7.4 Hz, 2H), 3.4 (m, 2H), 3.28 (m, 2H), 1.64 (m, 6H), 0.90 (t, J = 7.5 Hz, 3H). MS (FAB+) m/z: 445 [M + H+]. HRMS (FAB+): calculated for C$_{26}$H$_{29}$N$_4$O$_3$: 445.2240. Found: 445.2297.

2-Amino-N-(6-((1,3-dioxo-2-propyl-2,3-dihydro-1H-benzo[de] isoquinolin-6-yl)amino)hexyl)benzamide (3d). Yellow solid, 68.5 mg, 68% yield. FTIR: 3471, 3334, 3075, 2931, 1679, 1620, 1631, 1573, 1541 cm^{-1}. ^{1}H NMR (DMSO-d$_6$, 400 MHz): δ 8.71 (d, J = 8.5 Hz, 1H), 8.43 (d, J = 7.3 Hz, 1H), 8.26 (d, J = 8.6 Hz, 1H) 8.20 (t, J = 5.8 Hz, 1H), 7.79 (t, J = 5.6 Hz, 1H), 7.68 (t, J = 7.9, 1H), 7.44 (d, J = 7.9 Hz, 1H), 7.11 (t, J = 7.7 Hz, 1H), 6.78 (d, J = 8.6 Hz, 1H), 6.67 (d, J = 8.2 Hz, 1H), 6.49 (t, J = 7.4 Hz, 1H), 6.37 (s, 2H), 3.98 (t, J = 7.6 Hz, 2H), 3.36 (m, 2H), 3.21 (q, J = 6.7, 13.16 Hz, 2H), 1.71 (m, 2H), 1.63 (m, 2H), 1.53 (m, 2H), 0.91 (t, J = 7.4 Hz, 3H). ^{13}C NMR (DMSO-d$_6$, 101 MHz): δ 169.3, 164.3, 163.4, 151.1, 149.9, 134.8, 131.9, 131.1, 129.9, 129.0, 128.4, 124.6, 122.2, 120.5, 116.7, 115.6, 115.1, 107.9, 104.2, 43.3, 41.2, 29.6, 28.3, 26.9, 26.8, 21.4, 11.8. MS (FAB+) m/z: 473 [M + H$^+$]. HRMS (FAB+): calculated for C$_{28}$H$_{33}$N$_4$O$_3$: 473.2553. Found: 473.2528.

Synthesis of 2-propyl-6-(propylamino)-1H-benzo[de]iso-quinoline-1,3(2H)-dione (pp-ANAPIM). In a 50 mL round bottom flask with magnetic stirring compound **1** (300 mg, 0.63 mmol) was dissolved in DMF (10 mL) and propylamine was added dropwise (0.09 mL, 0.63 mmol). Then the reaction mixture was stirred at 110 °C for 3 h. After this time the solution was allowed to reach RT and poured into 100 mL of cold distilled water. Once a solid was observed, it was filtered and dried. The crude product was recrystallized in toluene to obtain a pure solid product. Yellow solid, 240 mg, 80% yield. ^{1}H NMR (DMSO-d$_6$, 400 MHz): δ 8.76 (d, J = 8.3 Hz, 1H), 8.48 (d, J = 7.2 Hz, 1H), 8.31 (d, J = 8.6 Hz, 1H), 7.86 (s, 1H), 7.80–7.67 (m, 1H), 6.83 (d, J = 8.6 Hz, 1H), 4.02 (t, J = 7.5 Hz, 2H), 3.42–3.31 (m, 2H), 1.89–1.56 (m, 4H), 1.06 (d, J = 7.4 Hz, 3H), 1.02–0.90 (m, 3H).

Synthesis of 2-amino-N-propylbenzamide (p-2ABZ). In a 50 mL round bottom flask with magnetic stirring isatoic anhydride (200 mg, 1.23 mmol) was dissolved in tetrahydro-furan (20 mL) under Ar atmosphere, the TEA (100 μL) was added to the solution. Once all reactives were dissolved, propylamine (1 molar equiv.) was added to the mixture and it was refluxed for 2 h. Finally, the solvent was removed under vacuum and the obtained solid was washed with petroleum ether (3 × 10 mL)

and ethyl ether (3 × 10 mL). White solid, 110 mg, 50% yield. ^{1}H NMR (DMSO-d$_6$, 400 MHz): δ 7.30 (dd, J = 7.7, 1.5 Hz, 1H), 7.20 (ddd, J = 8.2, 7.2, 1.5 Hz, 1H), 6.67 (d, J = 8.2 Hz, 1H), 6.64 (ddd, J = 7.9, 7.2, 1.2 Hz, 1H), 6.11 (s, 1H), 5.21 (brs, 2H), 3.37 (dt, J = 7.2, 5.8 Hz, 2H), 1.62 (sext, J = 7.2 Hz, 2H), 0.98 (t, J = 7.2 Hz, 3H).

Determination of quantum yields

Fluorescence quantum yields were measured using N-propyl 6-aminonaphthalimide in acetonitrile as standard with a known Φ_R of 0.58. Solutions of dyads **3a–d** and **pp-ANAPIM** were prepared at 5 × 10^{-6} M in spectroscopic grade acetonitrile. Absorbance and fluorescence spectra were measured, and the data required for eqn (1) were obtained from these spectra.

$$\Phi_s = \Phi_R \times \frac{I_s A_R n_s^2}{I_R A_s n_R^2} \tag{1}$$

where Φ_S is the sample quantum yield, Φ_R is the reference substance quantum yield; I_S and I_R are the area under the emission bands at a given wavelength range for the sample and reference, respectively; A_S and A_R are the absorbance value at the excitation wavelength (416 nm) for the sample and reference substance, respectively; n is the refractive index of the solvent.

Metal ion interaction study by UV-vis titrations

The effect of metal ions upon the absorbance was examined by adding 6 μL of a 1 × 10^{-3} M perchlorate salt solution to a known volume (3 mL) of a 1 × 10^{-5} M dyad solution. The dyad and perchlorate salt stock solutions were prepared in spectro-scopic grade acetonitrile. A quartz cuvette was filled with 3 mL of the dyad stock solution, then 6 μL aliquots of perchlorate salt stock solution were added successively with a calibrated micropipette. Thus, the ratio of the total concentration [salt]/[dyad] was in the desired range. The resulting complex solutions were stirred for 3 min, and the spectra were recorded. The absorption spectrum was confirmed to be unchanged with time at each measurement.

Metal ion interaction study by fluorometric titrations

The effect of metal ions upon the fluorescence emission was examined by adding 6 μL of a 5 × 10^{-3} M perchlorate salt solution to a known volume (3 mL) of a 5 × 10^{-5} M dyad solution. The dyad and perchlorate salt stock solutions were prepared in spectroscopic grade acetonitrile. A quartz cuvette was filled with 3 mL of dyad stock solution, then 6 μL aliquots of perchlorate salt stock solution were added successively with a calibrated micropipette. Thus, the ratio of the total concentration [salt]/[dyad] was in the chosen range. The resulting complex solutions were stirred for 3 min, and the spectra were recorded. The emission spectrum was confirmed to be unchanged with time at each measurement.

Computational methods

The calculations were carried out in two stages. First, a conformational search on the potential energy surfaces (PES) was done

for dyads **3a–d** using the basin hopping method, as it is implemented in the Tinker program.[26] The Merck Molecular force field (MMFF) was used in this step,[27] which shows a good performance in the conformational search for organic molecules.[28,29] For the obtained structures, additional geometry optimizations were performed using the B3LYP density functional, including dispersion correction (D3BJ) and using the def2-SVP basis set.[30–33] The implicit solvent effect was included through the polarizable continuum model using parameters corresponding to acetonitrile.[34] To quantify the relative contribution of each one of the conformers, the average of some properties was obtained using the Boltzmann distribution, considering the Gibbs free energies (from thermochemical calculations at 298 K) to calculate the weight factors.[35] The Time-Dependent Density Functional Theory (TDDFT) was employed to evaluate the electronic excited states.

In the second stage additional calculations were achieved in order to rationalize the excitation energy transfer (EET). Although formally the EET for dyads **3a–d** is an intramolecular process, the fragments 2ABZ and ANAPIM were analyzed individually as an acceptor and donor chromophores. For each relevant equilibrium geometry of the **3a–d** compounds, a pair of 2ABZ and ANAPIM moieties were obtained by eliminating the alkyl chain spacer and capping the free valence of each unit with one hydrogen atom. The position of the included H atom was determined by a constrained geometry optimization. Later, the electronic coupling term (V_{DA}) that appears in the expression of the EET rate was evaluated for the pairs 2ABZ–ANAPIM.[36–38] All the electronic structure calculations were performed using the Gaussian 16 program,[39] except the minimum energy conical intersections (MECI), which were obtained with the Q-Chem program.[40]

Results and discussion

Synthesis and characterization

The synthesis of 2ABZ–ANAPIM dyads (**3a–d**) is depicted in Scheme 1.

First, the *N*-propyl bromonaphthalimide **1** was prepared by a condensation reaction of 4-bromo-1,8-naphthalic anhydride with one molar equivalent of propylamine in refluxed ethanol with a 80% yield. Then, compound **1** was reacted with an excess of the corresponding alkyldiamine (**a–d**) in DMF obtaining the **2a–d** intermediates in good yields (41 to 86%). Finally, the amines **2a–d** were reacted with one molar equivalent of isatoic anhydride in dry THF obtaining **3a–d** in 68 to 80% yield.

The intermediates **1**, **2a–d** and dyads **3a–d** were characterized by ^{1}H and ^{13}C NMR, FTIR and MS (Fig. S1 to S30†). The FTIR spectrum of dyad **3a** shows the characteristic stretching vibrations for a primary and secondary amine, as well as amide groups from 3459 to 3300 cm^{-1}. The stretching vibrations of carbonyls are observed at 1677, 1631 and 1615 cm^{-1}. The bending vibration of N–H groups is at 1527 cm^{-1}. The spectra of **3b–3d** dyads show similar vibrations (see Table S1†).

The ^{1}H NMR spectrum of **1** obtained in DMSO-d$_6$ (Fig. 2a) shows the napththalimide AB system corresponding to H4 and H5 at 8.27 and 8.06 ppm. The signals for H8 and H6 are present
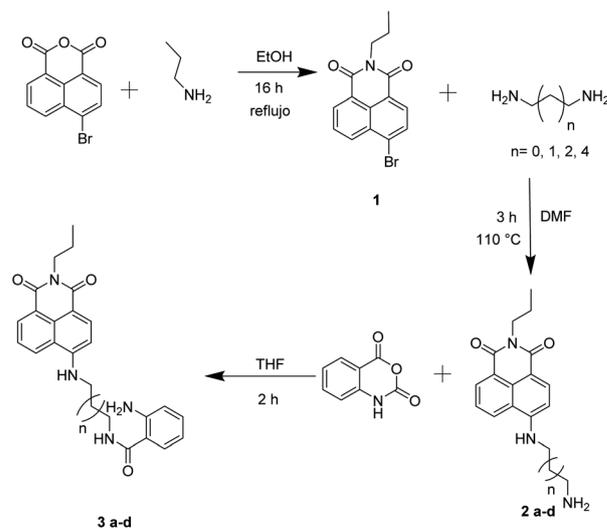
Scheme 1 Synthetic route for the synthesis of aminonapththalimide–aminobenzamide dyads.

at 8.52 and 8.48 ppm, and H7 is observed at 7.95 ppm. The aliphatic hydrogens H3 are located at 3.98 ppm, H2 at 1.64 ppm and H1 at 0.92 ppm. The spectrum of **2a** (Fig. 2b) shows the napththalimide AB system corresponding to H4 and H5 shifted to 8.24 and 6.85 ppm due to the protecting effect of the amino group over H5. The signals for H8 and H6 are observed at 8.62 and 8.44 ppm, respectively, and the signal for H7 is observed at 7.70 ppm. In addition to the dramatic chemical shift of H5 and H7, it is also significant the presence of new signals at 7.75 ppm and 3.47 ppm for the secondary amine and methylene hydrogens corresponding to the ethylenediamine chain, indicating a successful substitution of the bromine (Fig. S4†). The ^{1}H NMR spectrum of **3a** obtained in DMSO-d$_6$ (Fig. 2c) shows the signals for both ANAPIM and 2ABZ aromatic systems, amine, amide and aliphatic hydrogens. The AB system appears at 8.28 ppm and 6.93 ppm for H4 and H5, respectively. The signals for H8 and H7 are observed at 8.65 ppm and 7.71 ppm, while H6 appears at 8.45 ppm. The secondary amine hydrogen is observed at 7.94 ppm, while the amide hydrogen appears at 8.49 ppm. The 2ABZ aromatic hydrogens signals were observed at 7.48 ppm for H12, 6.21 ppm for H11, 7.14 ppm for H10 and 6.70 for H9. Also, it is present the signal for the amino-aromatic hydrogens at 6.46 ppm.

The ^{13}C NMR spectrum obtained in DMSO-d$_6$ of **2a** shows two signals at 163.4 and 162.4 ppm corresponding to the imide carbonyls (Fig. S5†). The ten signals of the ANAPIM system are observed from 151.0 to 104.0 ppm, the signals of the propyl group are at 43.0, 21.4 and 11.9 ppm, and the ethylene signals are at 41.2 and 36.6 ppm. The spectrum of **3a** (Fig. S18†) shows three signals for carbonyls at 170.0 (amide), 164.2 and 163.4 ppm (imide). There are sixteen signals for both ANAPIM and 2ABZ aromatic systems from 151.0 to 104.0 ppm. The propyl signals are present at 43.1, 21.4 and 11.9 ppm and the ethylene carbons are observed at 41.2 and 38.0 ppm. The assignment of the NMR signals for dyads **3a–d** are summarized in Tables S1 and S2.†
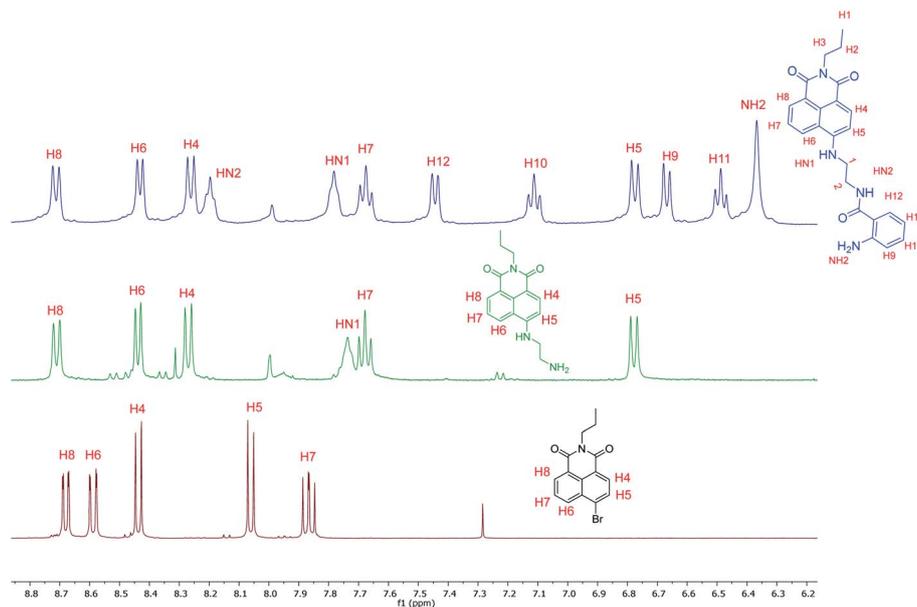
Fig. 2 ^{1}H NMR of **1** (A), **2a** (B) and **3a** (C).

Optical properties of ANAPIM-2ABZ dyads

In order to study the photophysical properties of dyads **3a–d**, the *N*-propyl 2-aminobenzamide (**p-2ABZ**) and 2-propyl-6-propylaminonaphthalimide (**pp-ANAPIM**) compounds were analyzed by UV-Vis and fluorescence spectroscopy. The UV-vis spectra of these compounds and dyads **3a–d** were analyzed in acetonitrile. The **p-2ABZ** electronic absorption band shows a maximum absorbance at 325 nm associated to a π–π* transition ($\varepsilon = 4370$ L mol^{-1} cm^{-1}), whilst the **pp-ANAPIM** band has three relative maximum peaks at 270, 296 and 420 nm, the latter also associated to a π–π* transition ($\varepsilon = 11\,327$ L mol^{-1} cm^{-1}) (Fig. 3A). Both chromophores behave an ICT process where the non-bonding electrons localized in nitrogen atoms (donors) are delocalized through the aromatic system to reach a carbonyl group (acceptors). The absorbance band of **3a** shows the characteristic peaks of the π–π* transition at 325 nm and 430 nm ($\varepsilon = 20\,530$ L mol^{-1} cm^{-1}) corresponding to 2ABZ and ANAPIM chromophores, respectively. Interestingly, the absorbance of ANAPIM chromophore increases in **3a** and a bathochromic shift (10 nm) is observed. The rest of dyads **3** have similar electronic absorption bands (Fig. S31†) and their ε values decrease as the spacer length increases (Table 1).

On the other hand, the fluorescence spectra of **p-2ABZ** have maximum excitation and emission at wavelengths of 325 nm and 391 nm, respectively. The **pp-ANAPIM** has a maximum excitation wavelength at 430 nm and the emission is at 517 nm. It is clearly observed that there is an overlap between the 2ABZ emission band and the ANAPIM excitation band. Interestingly, dyad **3a** shows a low intensity emission peak at 370 nm and high intensity emission peak at 519 nm when the molecule is excited at 325 nm (**p-2ABZ** excitation wavelength) indicating an energy transfer in the excited state from the 2ABZ to ANAPIM fluorophore. The intensity of the emission band at 325 nm

decreases as the alkyl spacer length increases in dyads **3a–d** (Fig. 3C), indicating a more efficient energy transfer. In addition, the quantum yield (Φ_F) of **pp-ANAPIM** is higher than those for **p-2ABZ** and dyads **3a–d** (Table 1), the lower Φ_F of dyads **3a–d** may be related to the efficiency in the energy transfer process.

The energy transfer efficiency (E_T) is related with the emission intensities of the donor–acceptor system (F_{DA}) and the donor emission intensity (F_D) in the eqn (2). Table 1 shows high E_T values in dyads **3a–d** (0.87 to 0.98) and there is a trend to increase as the alkyl spacer increases.

$$E_T = 1 - \frac{F_{DA}}{F_D} \qquad (2)$$

The overlap integral was calculated from the emission spectrum of **p-ABZ** (energy donor) and electronic absorption spectrum of **pp-ANAPIM** (energy acceptor) applying the Simpson 1/3 method to obtain a function for each spectrum (Fig. 4). Thus, a value of $J = 1.31 \times 10^{-13}$ J cm^3 L mol^{-1} was obtained from eqn (3).

$$J = \frac{\int f_D(\lambda)\varepsilon_A(\lambda)\lambda^4 d\lambda}{\int f_D(\lambda)d\lambda} = \int \overline{f_D}(\lambda)\varepsilon_A(\lambda)\lambda^4 d\lambda \qquad (3)$$

The Förster radius (R_0) is the distance between donor and acceptor, at which 50% of the energy transfer occurs, and it was calculated as 3.2 nm from eqn (4). The distance between both fluorophores in dyads **3a–d** was calculated using eqn (5). As can be seen in Table 1, all the *r* values are in the $0.5R_0 = 1.6 < r < 1.5R_0 = 4.8$ interval suggesting a favorable energy transfer process, and that the closer the fluorophores are to each other, the higher the energy transfer efficiency.
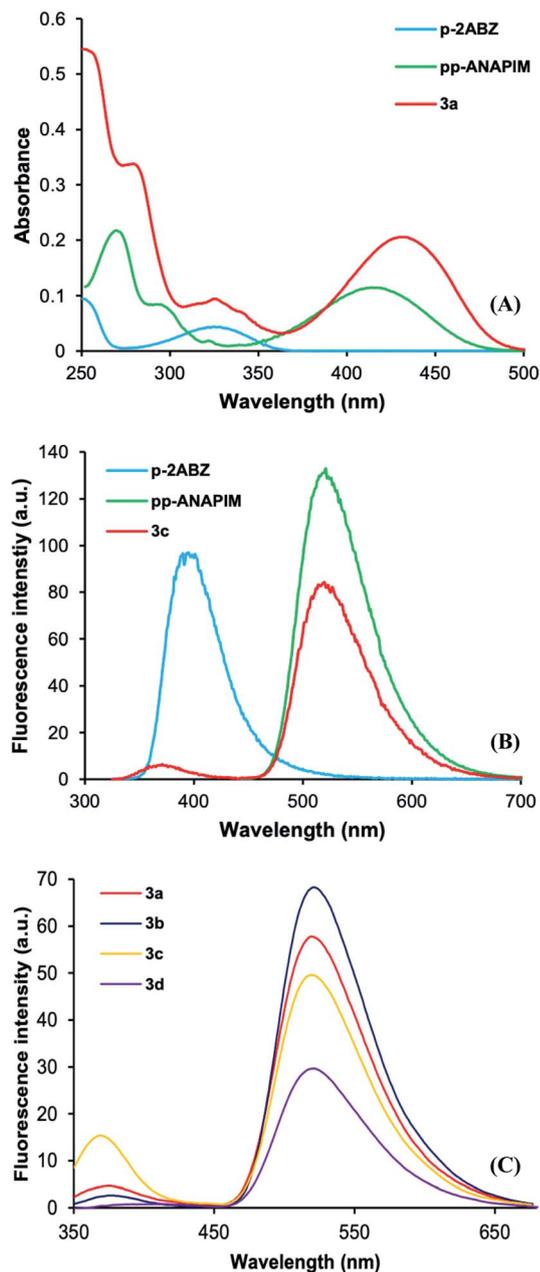
Fig. 3 (A) Electronic absorption spectra of **3a–d** obtained in aceto-nitrile at 1×10^{-5} M. (B) Emission spectra of **p-2ABZ**, **pp-ANAPIM** and **3a** obtained in acetonitrile at 5×10^{-5} M. (C) Emission spectra of dyads **3a–3d** (excited at 325 nm) obtained in acetonitrile at 5×10^{-5} M.

$$R_0^6 = 2.8 \times 10^{17} \cdot k^2 \cdot \Phi_D \cdot \varepsilon_A \cdot J \qquad (4)$$

$$E_T = \frac{1}{1 + (r/R_0)^6} \qquad (5)$$

Interaction of ANAPIM–2ABZ dyads with metal ions

The supramolecular interaction of dyads **3a–d** was studied experimentally by UV-vis spectrophotometric titrations in acetonitrile. In the experiments the concentration of dyads **3a–d** solutions was 1×10^{-5} M and titrations were achieved keeping their concentration constant and varying the metal ion

Table 1 Photophysical properties of dyads **3a–d**, **p-2ABZ** and **pp-ANAPIM**

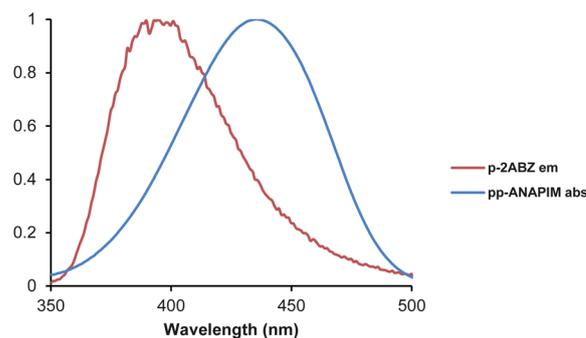| Compound	ε (L mol^{-1} cm^{-1})	E_T	r (nm)	Φ_F
3a	20 530	0.87	2.3	0.61
3b	18 387	0.93	2.1	0.65
3c	14 943	0.61	2.9	0.46
3d	14 361	0.98	1.7	0.47
p-2ABZ	4370			0.19
pp-ANAPIM	11 327			0.72

Fig. 4 Normalized emission spectrum of **p-2ABZ** (excited at 325 nm) and absorption spectrum of **pp-ANAPIM** obtained in acetonitrile at 5×10^{-5} M.

concentration by addition of aliquots of 1×10^{-3} M metal ion solutions.

The UV-vis titrations were performed using monovalent and divalent cations such as Li$^+$, Na$^+$, K$^+$, Mg^{2+}, Ca^{2+}, Hg^{2+}, Cu^{2+}, Cd^{2+}, Co^{2+} and Pb^{2+}. Interestingly, only Hg^{2+} and Cu^{2+} induced significant changes in the absorption band of these dyads. The titration of **3d** with Hg^{2+} (Fig. 5A) induced a hypochromic change in the band at 325 nm with an isosbestic point at 290 nm, indicating the interaction of the metal ion with the 2ABZ, while Cu^{2+} has a hyperchromic effect over the band from 250 to 390 nm probably due to the absorbance contribution of the Cu^{2+}-acetonitrile complex (Fig. S32†). However, there is a hypochromic change in the band at 430 nm with an isosbestic point at 395 nm. These changes are attributed to the inhibition of ICT processes by the coordination of Cu^{2+} with the amino groups of 2ABZ and ANAPIM chromophores. Besides the interaction with the cation induces a colorimetric change from green to colorless. The rest of dyads (**3a**, **3b**, **3c**) have the same behavior with Hg^{2+} and Cu^{2+} (Fig. S33 to S35†).

Based on the previous results, the titrations by fluorescence were conducted only with Hg^{2+} and Cu^{2+} ions in acetonitrile. Fig. 6 shows the spectra obtained from the titration with Cu^{2+} (A and B) and Hg^{2+} (C and D) exciting at 315 nm and 435 nm, respectively. As can be seen, there is a quenching of fluorescence by the coordination with these metal ions through the 2ABZ fluorophore inhibiting the ICT and hence the energy transfer (FRET) to the ANAPIM fluorophore. Also, these results suggest a coordination of the ions with the ANAPIM fragment inducing a quenching of fluorescence when the molecule is
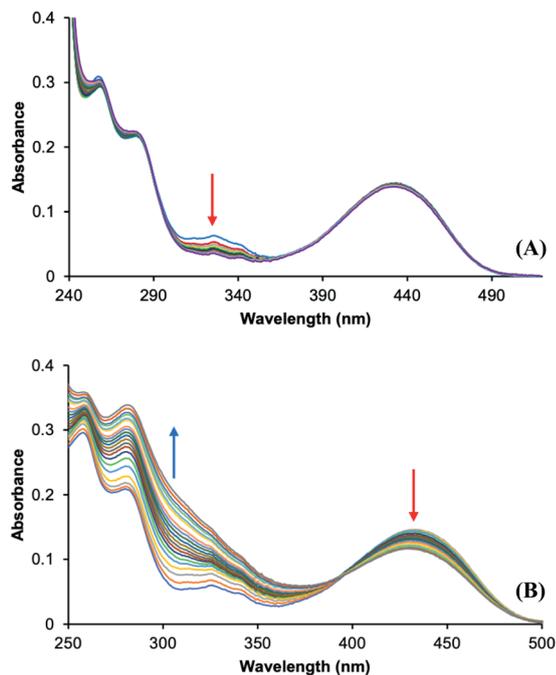
Fig. 5 Absorption spectra obtained by titration of dyad **3d** with Hg²⁺ (A) and Cu²⁺ (B) in acetonitrile. [**3d**] = 1 × 10⁻⁵ M.

excited at 435 nm. The rest of dyads (**3a**, **3b**, **3c**) have a similar behavior (Fig. S36 to S38†).

In order to corroborate the interaction of the ANAPIM moiety with the metal ions, the fluorescent behavior of **pp-ANAPIM** with Hg²⁺ and Cu²⁺ was analyzed (Fig. 6). The titration with Hg²⁺ shows a significant fluorescence quenching, while only a slight

effect was observed with Cu²⁺ (Fig. S39†). This means that Cu²⁺ complexes with dyads **3** require the interaction of both 2ABZ and ANAPIM fragments to establish a cooperative coordination. Noteworthy, the quenching of fluorescence was more intense in dyad **3d**, which has the longest alkyl chain between both fluorophores, while dyads **3a–c** have a similar quenching behavior (Fig. S40 and Table S4†).

The Stern–Volmer constants (K_{SV}) were determined for those complexes with Cu²⁺ and Hg²⁺ (Table 2) using eqn (6), where F_0 is the free dyad fluorescence intensity, F is the fluorescence intensity in presence of the metal ion and [C] is the metal ion concentration.

$$\frac{F_0}{F} = 1 + K_{SV}[C] \tag{6}$$

All the Stern–Volmer graphs were linear on the 0 to 150 μM interval of cation added, suggesting only one type of quenching (Fig. S41 to S44†). Considering that titrations by UV-Vis show the formation of a complex in the ground state, it is proposed a static quenching in these complexes. The K_{SV} values corroborate the finding trend observed in the experimental study, showing more sensibility towards Hg²⁺ than Cu²⁺ in all days, however, the $K_{SV}(Hg^{2+})/K_{SV}(Cu^{2+})$ ration indicates that the sensibility towards Cu²⁺ increases as the alkyl spacer are longer. Finally, the higher K_{SV} were obtained for the complexes with dyad **3d**.

Theoretical analysis of ANAPIM–2ABZ dyads photophysical properties

To rationalize the experimental findings corresponding to the photophysical behavior of dyads **3a–d**, the starting point was to
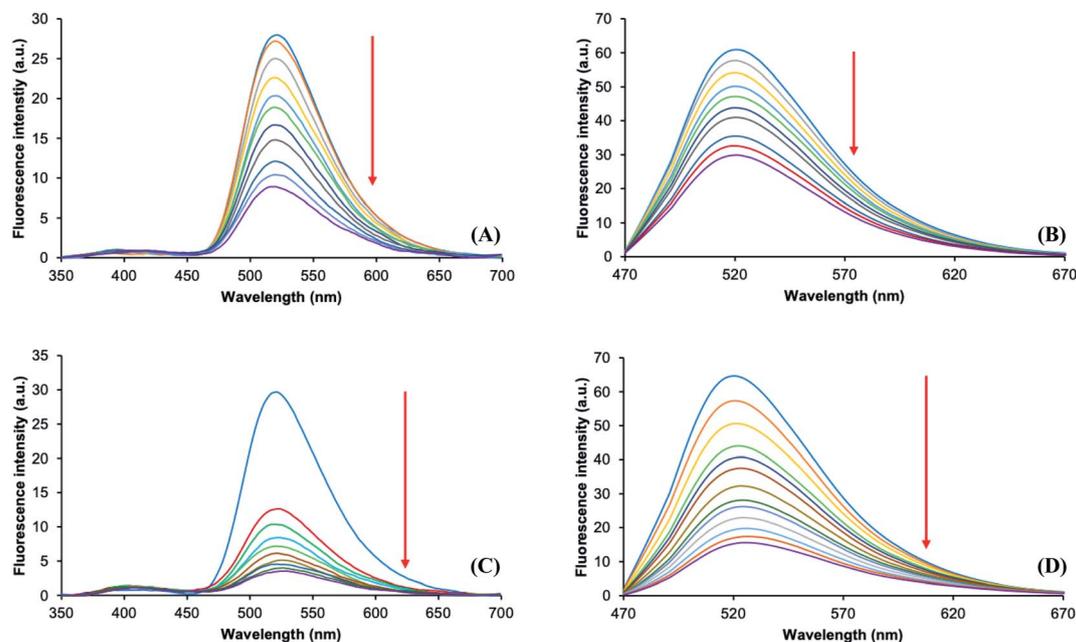

Fig. 6 Emission spectra obtained by titration of dyad **3d** with Cu²⁺ exciting at 315 nm (A) and at 435 nm (B) in acetonitrile. Emission spectra obtained by titration of dyad **3d** with Hg²⁺ exciting at 315 nm (C) and at 435 nm (D) in acetonitrile. [**3d**] = 5 × 10⁻⁵ M.

Table 2 Stern–Volmer constants (K_{SV}) for complexes with dyads **3a–d**

M^{n+}	3a	3b	3c	3d
Hg^{2+}, λ_{ex}: 315 nm	3.79×10^4 M^{-1} ($R^2 = 0.99$)	3.30×10^4 M^{-1} ($R^2 = 0.99$)	3.13×10^4 M^{-1} ($R^2 = 0.99$)	5.51×10^4 M^{-1} ($R^2 = 0.95$)
Cu^{2+}, λ_{ex}: 315 nm	3.30×10^3 M^{-1} ($R^2 = 0.95$)	3.40×10^3 M^{-1} ($R^2 = 0.94$)	3.50×10^3 M^{-1} ($R^2 = 0.97$)	1.55×10^4 M^{-1} ($R^2 = 0.98$)
$K_{SV}(Hg^{2+})/K_{SV}(Cu^{2+})$	11.5	9.7	8.9	3.6

find the global minima of the PES for these compounds, as well as all the thermally accessible structures at 298 K, in accordance with the experimental conditions. Fig. 7 shows the structures obtained for the global minima of **3a–d**, where the stacking of both fluorophores 2ABZ and ANAPIM is observed for all dyads. Additionally, at 298 K only a few conformations show a relevant contribution according to the calculated Boltzmann factors, and in almost the cases, for these structures we observed the stacking among the aromatic rings (Fig. S45†).

The ESI† includes the simulated electronic absorption and emission spectra for **p-2ABZ** and **pp-ANAPIM** (Fig. S46†), as well as the related dealkylated compounds (Fig. S47†). In general, there is a good match between the experimental and the simulated spectra, although the theoretical values are slightly shifted to lower wavelength. For example, for the $S_0 \rightarrow S_1$ electronic transition of **p-2ABZ** and **pp-ANAPIM** the maximum of the bands are centered at 312 and 416 nm, against the experimental values of 326 and 420 nm, respectively. Also, the analysis of the TDDFT amplitudes reveals that for **p-2ABZ** and **pp-ANAPIM** the S_1 state can be ascribed as $^1\pi\pi^*$ nature, and also, the excited state of both molecules is well described by a single HOMO–LUMO configurational change.

The simulated electronic absorption spectra for dyads **3a–d** are also similar to the experimental data (Fig. S48†). In these molecules the interaction between the chromophores causes a splitting of the S_1 states of each individual fragment, giving rise to four singlet electronic states for the dyad. From these, two involve small oscillator forces and do not contribute

significantly to the absorption spectra. A comparison of Fig. S46 and S48† suggests that the stacking interactions does not affect considerably the electronic transitions of chromophores 2ABZ and ANAPIM in dyads **3a–d** because of the maximum absorbance wavelengths are nearly the same to those observed in **p-2ABZ** and **pp-ANAPIM**. In dyads **3a–d**, the HOMO and HOMO−1 are constituted by the bonding and antibonding combination of the HOMOs of base chromophores, whilst the LUMO is centered at the ANAPIM chromophore and the LUMO+1 in 2ABZ (Fig. S49†). The lowest energy electronic transitions in **3a–d** are described by significant amplitudes which involve the configurational changes between HOMO−1/HOMO and LUMO+1/LUMO, so is possible classify the electronic states as associated with the formation of an exciplex (π-complex).

The relative position of the electronic states, modulated by the conformation, has important consequences in the photophysical behavior of dyads **3a–d**. For example, Fig. 8 shows the minimum energy path (MEP) for two different conformations of dyad **3a**. In both cases, the photophysical pathway begins from an equilibrium geometry of S_0 and the transition takes place towards the second bright electronic state. As can be seen, in the stacked conformation the MEP starts in S_4, and the reaction profile proceeds from the Franck–Condon region towards the minimum of S_1. Only a small barrier of 0.013 eV needs to be surpassed in order to access to an S_3/S_2 MECI. Since the initial absorption $S_0 \rightarrow S_4$ occurs at 322 nm, while the $S_3 \rightarrow S_0$ and $S_1 \rightarrow S_0$ emissions from the respective minimums take place at
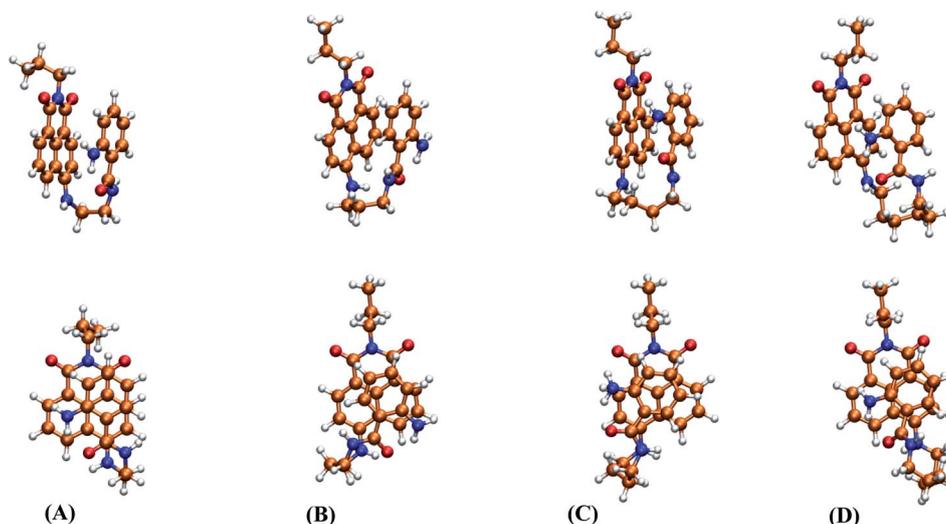

Fig. 7 Side and front views for the molecular structures corresponding to the global minima of the PES for **3a** (A), **3b** (B), **3c** (C) and **3d** (D).
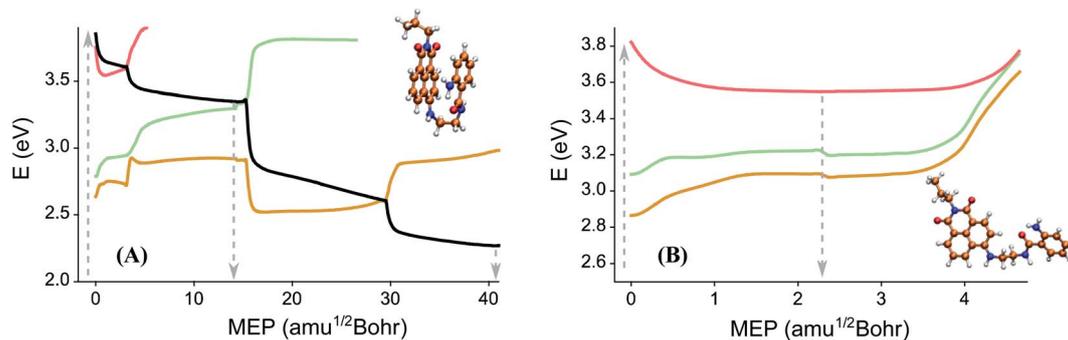
Fig. 8 Energy of the first singlet electronic states along the minimum energy path in the exciting state of stacked (A) and folded (B) conformations of **3a**. The vertical dotted lines denote a vertical transition from/to S_0.

412 and 480 nm, conceptually this process may be interpreted as an energy transfer from the 2ABZ towards the ANAPIM system. Noteworthy, the PES crossings S_4/S_3, S_3/S_2 and S_2/S_1 take place along the MEP.

On the other hand, for the folded conformation the process starts at $S_0 \rightarrow S_3$, and the MEP evolves to a minimum of S_3. From this region is necessary to overcome a barrier of 0.25 eV to access to an S_3/S_2 MECI. Also, the emission $S_3 \rightarrow S_0$ from the minimum of S_3 is about 375 nm. Since this value is pretty similar to the maximum wavelength of the 2ABZ emission spectrum, it may be considered that it the folded conformation the energy is localized at the same chromophore. We also calculate the MEP for the global minima of dyad **3d** and the same behavior as the stacked conformation of **3a** was obtained (Fig. S50†). In other words, the stacked conformations favor the internal conversion process and in consequence, the EET. As the most stable conformations in dyads **3a–d** involve stacked arrangements, the MEP data allow to rationalizing mechanistically the high energy transfer efficiencies observed experimentally.

With the purpose of explain the observed trend in the fluorescence quantum yields along the series of dyads **3a–d**, the electronic couplings for the acceptor–donor pairs were calculated and are presented in Table 3. Briefly, the EET rate is given by $k_{EET} = \pi V_{DA}^2 J/\hbar$,[38] where J corresponds to the overlap integral of the normalized emission and absorption spectra of the donor and acceptor, respectively. The coupling is given by the addition of all the coulombic contributions (Förster type), exchange–correlation (Dexter type), the overlap part and a term associated with the solvent, such that $V_{DA} = V^{coul} + V^{XC} + V^{over} + V^{PCM}$. Dyads **3a–d** have the same J value, and hence, as higher is V_{DA} higher is the energy transfer ratio. The R column in Table 3 denotes the distance between the geometric center of 2ABZ and the central carbon of ANAPIM system. In general, the values of V_{DA} are high in all dyads and agree with the high energy transfer ratios as result of the closeness of chromophores in the stacked conformations. Also, the coulombic term makes the biggest contribution to the coupling. Although these values are consistent, they do not allow to explain the trend along the series, since according to experimental data a bigger magnitude of V_{DA} for **3d** would be expected, whilst is the smaller for **3c**.

Theoretical study of supramolecular complexes of dyads 3a–d with metal ions

The formation of supramolecular complexes of dyads **3a–d** and metal ions induces significant changes in their structural and photophysical properties. In order to find the mechanisms responsible for these changes the complexes with Cu^{2+} and Hg^{2+} were theoretically studied. As can be seen in Fig. 9 and 10, an imide carbonyl of ANAPIM and the amino and amide carbonyl of 2ABZ interact with the metal ion (also see Fig. S51 and S52†) disrupting the stacking of the aromatic fragments observed in the free ligands. Although it was possible to find structures in which one of the NHR2 from the polymethylene bridge is bonded to the metal, the associated electronic energies (and also the free energies) are significantly higher with regard to the energy of the global minimum, so they are not relevant for the present analysis. Table 3 shows that the R values for the donor–acceptor fragments are higher in these metallic complexes. The simulated electronic absorption spectra for the complexes with Cu^{2+} and Hg^{2+} also agree with the experimental data, particularly, present absorbance band at positions similar to those for **p-2ABZ** and **pp-ANAPIM**.

Table 3 Electronic coupling for the energy transfer between the donor and acceptor chromophores in dyads **3a–d**. The first-row data corresponds to free dyads and the second and third to the complexes formed with Cu^{2+} and Hg^{2+}, respectively. The R value denotes the distance between the geometric center of 2ABZ and the central carbon of ANAPIM

| Dyad	R	V^{coul}	V^{XC}	V^{over}	V^{PCM}	V_{DA}
3a	3.3847	0.0666	−0.0006	0.0000	−0.0154	0.0503
	4.8670	0.0217	0.0001	0.0000	−0.0065	0.0154
	5.1732	0.0264	0.0000	0.0000	−0.0081	0.0184
3b	3.2382	0.0532	−0.0001	0.0000	−0.0133	0.0398
	7.1545	0.0158	0.0000	0.0000	−0.0055	0.0102
	7.3772	0.0182	0.0000	0.0000	−0.0062	0.0119
3c	3.1503	0.0585	−0.0003	0.0000	−0.0146	0.0433
	7.1578	0.0076	0.0000	0.0000	−0.0027	0.0048
	7.2732	0.0100	0.0000	0.0000	−0.0034	0.0066
3d	3.7338	0.0512	−0.0004	0.0000	−0.0126	0.0369
	7.4223	0.0054	0.0000	0.0000	−0.0020	0.0034
	7.8098	0.0074	0.0000	0.0000	−0.0026	0.0047
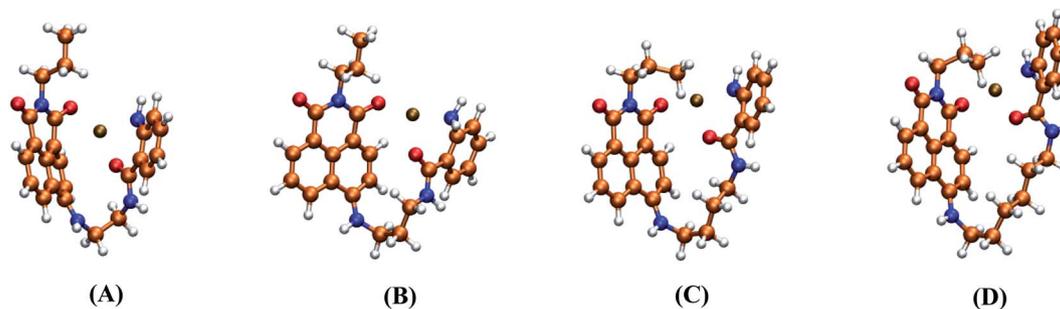
Fig. 9 Lateral view of molecular structures corresponding to the global minimum for the complexes with Cu^{2+} and dyads **3a** (A), **3b** (B), **3c** (C) and **3d** (D). The ground state spin multiplicity corresponds to $S = 1$.

However, for the supramolecular complexes the description of the electronic states is even more elaborated. Fig. S53† shows the frontier molecular orbitals (MO) for **3b-Hg²⁺** complex, this system presents a singlet spin multiplicity for the ground state. Comparing the MO of the complex and free ligand as well the amplitude information, it is possible to assign the nature of the electronic states for the complex. The configurational changes HOMO/LUMO and HOMO−1/LUMO+2 of **3b-Hg²⁺** are similar to the HOMO/LUMO of **p-2ABZ** and **pp-ANAPIM**. In fact, the S_1 electronic state of **3b-Hg²⁺** is well described by the configurational change HOMO/LUMO and the transition $S_0 \rightarrow S_1$ is localized in the ANAPIM fragment. This is also corroborated by analysis of the natural transition orbitals. Importantly, the electronic states of the complex described by the change HOMO−1/LUMO+1 and HOMO−1/LUMO+2 that would be involved in the excitation process localized in the 2ABZ system appear shifted to higher energy (¡S_{13} and S_{15}!), so the respectively electronic transition from the ground state takes place approximately at 274 nm. This result agrees with the spectroscopic changes observed in the electronic absorption spectra of **3b-Hg²⁺** complex, where there is a hypochromic effect at 320 nm and hyperchromic change before 270 nm.

For **3b-Cu²⁺**, the ground state spin multiplicity corresponds to a doublet. Unlike the complex with Hg^{2+} which has a filled d layer and where the d occupied orbitals are localized in the metal center, in **3d-Cu²⁺** exists a significant mixing of the molecular orbitals of the ANAPIM system and d-orbitals of the metal ion (Fig. S54†). In fact, the electronic state described by

the configurational change $HOMO_{\alpha}/LUMO_{\alpha}$, which would be associated to the transition localized in ANAPIM system corresponds to S_{14}. The analysis of the natural transition orbital reveals that the transitions toward lower energy states, which extend to the infrared zone, correspond to the metal–ligand excitations (Fig. S55†). Also, the electronic state where the excitation is localized in 2ABZ system is shifted to higher energy with regard to the free ligand. In general, the interaction of dyads **3a–d** with metal ions considerably changes the electronic structure of these molecules and the mechanism of fluorescence quenching is different to the observed in the ligands. Due to the closeness of the electronic energies and the huge density of states in the supramolecular complexes, it is possible to consider the intersystem crossover towards $S_1(D_0)$ may be favored according to the Kasha rule.[41] The above was corroborated with geometry optimizations for **3b-Hg²⁺** and **3b-Cu²⁺** complexes. For example, in the searching of the minimum for S_4 state (absorption at 324 nm) for **3b-Hg²⁺**, the energy of the excited state decreases considerably, after seven or eight iterations changes to be S_1. Interestingly, along this process the complexation with Hg^{2+} is disrupted releasing the metal ion and providing an unfolded dyad.

In summary, the data obtained by theoretical calculations suggest that in the complexes with Cu^{2+} and Hg^{2+} the excitation at 325 nm leads to an excited state different to the observed in free dyads. Very interestingly, the intensity decreases of the emission band at 530 nm by increasing the amount of metal ion in the solution, may be due to internal conversion toward
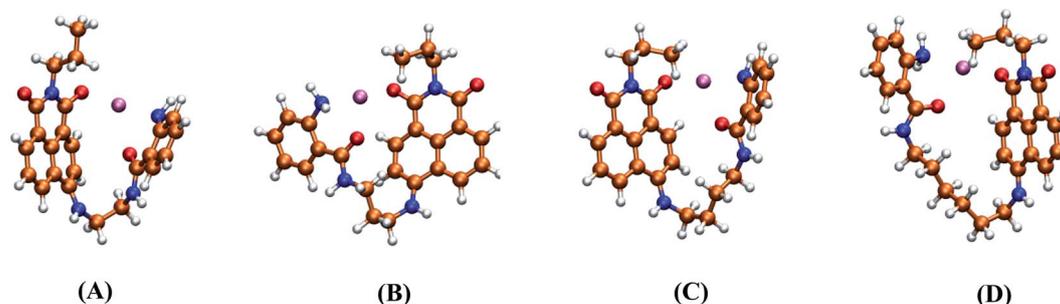

Fig. 10 Lateral view of molecular structures corresponding to the global minimum for the complexes with Hg^{2+} and dyads **3a** (A), **3b** (B), **3c** (C) and **3d** (D). The ground state spin multiplicity corresponds to $S = 0$.

inferior electronic states; in other words, the calculations suggest that both metal complexes should emit fluorescence in the near infrared.

Conclusions

The experimental and theoretical studies demonstrated a very efficient FRET process present in 2ABZ–ANAPIM fluorescent dyads. This is due to an overlap of the 2ABZ emission energy with the ANAPIM absorption energy, also the flexible interconnection between both fluorophores allows the stacking configuration, even with the shortest spacer, although with the longest the stacking is more favored. In mechanistic terms, the high FRET ratios showed by the dyads are consistent with the calculated barrierless MEP's, that lead directly from the state initially populated by light absorption toward the minimum of the first excited state, all through accessible crossings between the different potential energy surfaces. Additionally, the calculation of the EET couplings between the donor and acceptor chromophores are consistent with these results. The fluorescence quenching in the presence of Cu^{2+} and Hg^{2+} indicates the interaction with these metal ions inhibiting the FRET process between both fluorophores and their individual ICT processes, suggesting a cooperative interaction of both fluorophores. The optimization of the complexes geometry showed the interaction through the amine and carbonyl groups in 2ABZ and a carbonyl of ANAPIM, keeping the fluorophores away and changing their configuration and optical properties.

Author contributions

A. L. G.: investigation. A. O.-T.: conceptualization, resources, formal analysis, funding acquisition, writing – original draft preparation. A. T.-G.: conceptualization, investigation. J. J.-C.: conceptualization, resources, formal analysis, writing – original draft preparation. G. P.-L.: conceptualization, writing-reviewing and editing. H. S. O.: investigation, resources. V. L.-G.: investigation, resources. M. O.: investigation, resources. J. P.: resources, writing-reviewing and editing.

Conflicts of interest

There are no conflicts to declare.

Acknowledgements

Notes and references

1 United Nations, Department of Economic and Social Affairs, Population Division, World Population Prospects 2019: Methodology of the United Nations population estimates and projections, 2019.

2 United Nations Educational, Scientific and Cultural Organization (UNESCO), The United Nations World Water Development Report 2019, Leaving No One Behind.

3 S. Atilgan, T. Ozdemir and E. U. Akkaya, *Org. Lett.*, 2010, **12**, 4792–4795.

4 S. Sarma, B. Devi, P. K. Bhattacharyya and D. K. Das, *J. Fluoresc.*, 2020, **30**, 1513–1521.

5 J. A. Cotruvo Jr, A. T. Aron, K. M. Ramos-Torresa and C. J. Chang, *Chem. Soc. Rev.*, 2015, **44**, 4400–4414.

6 X. Q. Chen, T. Pradhan, F. Wang, J. S. Kim and J. Yoon, *Chem. Rev.*, 2012, **112**, 1910–1956.

7 J. H. Jung, J. H. Lee and S. Shinkai, *Chem. Soc. Rev.*, 2011, **40**, 4464–4474.

8 M. Martinez-Quiroz, X. E. Aguilar-Martinez, M. T. Oropeza-Guzman, R. Valdez and E. A. Lopez-Maldonado, *Molecules*, 2019, **24**, 1737.

9 T. Gunnlaugsson, P. E. Kruger, T.-C. Lee, R. Parkesh, F. M. Pfeffer and Y. M. Hussey, *Tetrahedron Lett.*, 2003, **44**, 6575–6578.

10 S. Anbu, A. Paul, K. Surendranath, A. Sidali and A. J. L. Pombeiro, *J. Inorg. Biochem.*, 2021, **220**, 111466.

11 M. S. Kim and T. Tsukahara, *ACS Earth Space Chem.*, 2020, **4**, 2270–2280.

12 N. I. Georgiev, P. V. Krasteva and V. B. Bojinov, *J. Lumin.*, 2019, **212**, 271–278.

13 L. Wang, Y.-Q. Fan, X.-W. Guan, W.-J. Qu, Q. Lin, H. Yao, T.-B. Wei and Y.-M. Zhang, *Tetrahedron*, 2018, **74**, 4005–4012.

14 N. Saini, N. Prigyai, C. Wannasiri and V. Ervithayasuporn, *J. Photochem. Photobiol., A*, 2018, **358**, 215–225.

15 K. Shen, S. Mao, X. Shi, F. Wang, Y. Xu, S. Opeyemi Aderinto and H. Wu, *Luminiscence*, 2017, **33**, 54–63.

16 H. Zhang, Y. Qu, K. Zhao, C. Wang, Y. Wu and H. A Wu, *J. Chin. Chem. Soc.*, 2020, **67**, 1062–1069.

17 P. A. Pachenko, Y. V. Fedorov, O. A. Fedorova and G. Jonusauskas, *Dyes Pigm.*, 2013, **98**, 347–357.

18 B. Dong, X. Song, C. Wang, X. Kong, Y. Tang and W. Lin, *Anal. Chem.*, 2016, **88**, 4085–4091.

19 M. Landey-Álvarez, A. Ochoa-Terán, G. Pina-Luis, M. Martínez-Quiroz, M. Aguilar-Martínez, J. Elías-García, V. Miranda-Soto, J. Ramírez, L. Machi-Lara, V. Labastida-Galván and M. Ordoñez, *Supramol. Chem.*, 2016, **28**, 893–906.

20 V. Ravindar, S. J. Swamy, S. Srihari and P. Lingaiah, *Polyhedron*, 1985, **4**, 1511–1518.

21 J. Dharmaraja, T. Esakkidurai, P. Subbaraj and S. Shobana, *Spectrochim. Acta, Part A*, 2013, **114**, 607–621.

22 J. Dharmaraja, P. Subbaraj, T. Esakkidurai and S. Shobana, *Spectrochim. Acta, Part A*, 2014, **132**, 604–614.

23 S. Abad, M. Kluciar, M. A. Miranda and U. Pischel, *J. Org. Chem.*, 2005, **70**, 10565–10568.

24 B. H. Shankar and D. Ramaiah, *J. Phys. Chem. B*, 2011, **115**, 13292–13299.

25 V. S. Jisha, A. J. Thomas and D. Ramaiah, *J. Org. Chem.*, 2009, **74**, 6667–6673.

26 J. A. Rackers, Z. Wang, C. Lu, M. L. Laury, L. Lagardère, M. J. Schnieders, J.-P. Piquemal, P. Ren and J. W. Ponder, *J. Chem. Theory Comput.*, 2018, **14**, 5273–5289.

27 T. A. Halgren, *J. Comput. Chem.*, 1996, **17**, 490–519.

28 T. A. Halgren and R. B. Nachbar, *J. Comput. Chem.*, 1996, **17**, 587–615.

29 T. Lewis-Atwell, A. Townsend Piers and N. Grayson Matthew, *Tetrahedron*, 2021, **79**, 131865.

30 A. D. Becke, *J. Chem. Phys.*, 1993, **98**, 5648–5652.

31 P. J. Stephens, F. J. Devlin, C. F. Chabalowski and M. J. Frisch, *J. Phys. Chem.*, 1994, **98**, 11623–11627.

32 F. Weigend and R. Ahlrichs, *Phys. Chem. Chem. Phys.*, 2005, **7**, 3297–3305.

33 S. Grimme, S. Ehrlich and L. Goerigk, *J. Comput. Chem.*, 2011, **32**, 1456–1465.

34 J. Tomasi, B. Mennucci and R. Cammi, *Chem. Rev.*, 2005, **105**, 2999–3094.

35 G. Barone, D. Duca, A. Silvestri, L. Gomez-Paloma, R. Riccio and G. Bifulco, *Chem.–Eur. J.*, 2002, **8**, 3240–3245.

36 C. Curutchet and B. Mennucci, *J. Am. Chem. Soc.*, 2005, **127**, 16733–16744.

37 M. F. Iozzi, B. Mennucci, J. Tomasi and R. Cammi, *J. Chem. Phys.*, 2004, **120**, 7029–7040.

38 C. Azarias, R. Russo, L. Cupellini, B. Mennucci and D. Jacquemin, *Phys. Chem. Chem. Phys.*, 2017, **19**, 6443–6453.

39 M. J. Frisch, G. W. Trucks, H. B. Schlegel, G. E. Scuseria, M. A. Robb, J. R. Cheeseman, G. Scalmani, V. Barone, G. A. Petersson, H. Nakatsuji, X. Li, M. Caricato, A. V. Marenich, J. Bloino, B. G. Janesko, R. Gomperts, B. Mennucci, H. P. Hratchian, J. V. Ortiz, A. F. Izmaylov, J. L. Sonnenberg, D. Williams-Young, F. Ding, F. Lipparini, F. Egidi, J. Goings, B. Peng, A. Petrone, T. Henderson, D. Ranasinghe, V. G. Zakrzewski, J. Gao, N. Rega, G. Zheng, W. Liang, M. Hada, M. Ehara, K. Toyota, R. Fukuda, J. Hasegawa, M. Ishida, T. Nakajima, Y. Honda, O. Kitao, H. Nakai, T. Vreven, K. Throssell, J. A. Montgomery Jr, J. E. Peralta, F. Ogliaro, M. J. Bearpark, J. J. Heyd, E. N. Brothers, K. N. Kudin, V. N. Staroverov, T. A. Keith, R. Kobayashi, J. Normand, K. Raghavachari, A. P. Rendell, J. C. Burant, S. S. Iyengar, J. Tomasi, M. Cossi, J. M. Millam, M. Klene, C. Adamo, R. Cammi, J. W. Ochterski, R. L. Martin, K. Morokuma, O. Farkas, J. B. Foresmany and D. J. Fox, *Gaussian 16, Revision C.01*, Gaussian Inc., Wallingford CT, 2016.

40 Y. Shao, Z. Gan, E. Epifanovsky, A. T. B. Gilbert, M. Wormit, J. Kussmann, A. W. Lange, A. Behn, J. Deng, X. Feng, D. Ghosh, M. Goldey, P. R. Horn, L. D. Jacobson, I. Kaliman, R. Z. Khaliullin, T. Kuś, A. Landau, J. Liu, E. I. Proynov, Y. Min Rhee, R. M. Richard, M. A. Rohrdanz, R. P. Steele, E. J. Sundstrom, H. L. Woodcock III, P. M. Zimmerman, D. Zuev, B. Albrecht, E. Alguire, B. Austin, G. J. O. Beran, Y. A. Bernard, E. Berquist, K. Brandhorst, K. B. Bravaya, S. T. Brown, D. Casanova, C.-M. Chang, Y. Chen, S. H. Chien, K. D. Closser, D. L. Crittenden, M. Diedenhofen, R. A. DiStasio Jr, H. Do, A. D. Dutoi, R. G. Edgar, S. Fatehi, L. Fusti-Molnar, A. Ghysels, A. Golubeva-Zadorozhnaya, J. Gomes, M. W. D. Hanson-Heine, P. H. P. Harbach, A. W. Hauser, E. G. Hohenstein, Z. C. Holden, T.-C. Jagau, H. Ji, B. Kaduk, K. Khistyaev, J. Kim, J. Kim, R. A. King, P. Klunzinger, D. Kosenkov, T. Kowalczyk, C. M. Krauter, K. Un Lao, A. D. Laurent, K. V. Lawler, S. V. Levchenko, C. Yeh Lin, F. Liu, E. Livshits, R. C. Lochan, A. Luenser, P. Manohar, S. F. Manzer, S.-P. Mao, N. Mardirossian, A. V. Marenich, S. A. Maurer, N. J. Mayhall, E. Neuscamman, C. M. Oana, R. Olivares-Amaya, D. P. O'Neill, J. A. Parkhill, T. M. Perrine, R. Peverati, A. Prociuk, D. R. Rehn, E. Rosta, N. J. Russ, S. M. Sharada, S. Sharma, D. W. Small, A. Sodt, T. Stein, D. Stück, Y.-C. Su, A. J. W. Thom, T. Tsuchimochi, V. Vanovschi, L. Vogt, O. Vydrov, T. Wang, M. A. Watson, J. Wenzel, A. White, C. F. Williams, J. Yang, S. Yeganeh, S. R. Yost, Z.-Q. You, I. Ying Zhang, X. Zhang, Y. Zhao, B. R. Brooks, G. K. L. Chan, D. M. Chipman, C. J. Cramer, W. A. Goddard III, M. S. Gordon, W. J. Hehre, A. Klamt, H. F. Schaefer III, M. W. Schmidt, C. D. Sherrill, D. G. Truhlar, A. Warshel, X. Xu, A. Aspuru-Guzik, R. Baer, A. T. Bell, N. A. Besley, J.-D. Chai, A. Dreuw, B. D. Dunietz, T. R. Furlani, S. R. Gwaltney, C.-P. Hsu, Y. Jung, J. Kong, D. S. Lambrecht, W. Liang, C. Ochsenfeld, V. A. Rassolov, L. V. Slipchenko, J. E. Subotnik, T. Van Voorhis, J. M. Herbert, A. I. Krylov, P. M. W. Gill and M. Head-Gordon, *Mol. Phys.*, 2015, **113**, 184–215.

41 N. J. Turro, V. Ramamurthy and J. Scaiano, *Modern Molecular Photochemistry of Organic Molecules*, University Science Books, 2010.